Theoretical evidence for unexpected O-rich phases at corners of MgO surfaces

Saswata Bhattacharya[1], Daniel Berger[2], Karsten Reuter[2], L. M. Ghringhelli[3], Sergey V. Levchenko[3]
[1] *Department of Physics, Indian Institute of Technology Delhi, Hauz Khas, New Delhi 110016, India*
[2] *Chair for Theoretical Chemistry and Catalysis Research Center, Technical University Munich, Lichtenbergstr. 4, D-85747 Garching, Germany*
[3] *Fritz-Haber-Institut der Max-Planck-Gesellschaft, Faradayweg 4-6, D-14195 Berlin, Germany*
(Dated: September 27, 2017)

Supplemental Material

1. Different types of embedded MgO corners
2. Convergence of 4×4×2@8×8×2 size for the periodic model
3. The QM/MM model: MM parameter optimization and convergence w.r.t. to cluster size
4. Validation of QM/MM model calculations w.r.t periodic boundary calculations
5. Phase diagrams for unembedded clusters
6. Concentration of defects and error estimation for μ_e=± 0.2 eV

I. Different types of embedded MgO corners

Using our massively parallel cascade genetic algorithm [1, 2], we found that for all defects global minimum structures have the defect located at the O-terminated corner and not at the edges or faces of the parallelepipedal structures. The greater stability of the oxygen ad-species at the O- versus Mg-terminated corner is explained by the stronger basicity of the undercoordinated O atom that can donate electrons to the additional electrophilic O species.

The initial geometries for the embedded clusters are created by cutting out the defected corner (for the excess of O atoms at the corner x = -1, 1 and 2 relative to the pristine O-terminated corner, see main text) and its nearest neighbors from the isolated parallelepipedal clusters and replacing it with the corresponding part at the corner of interest of the otherwise perfect embedded cluster. The number of relaxed atoms in the QM region were expanded until the convergence of the formation energies of the defects is achieved. Similarly, convergence of electrostatic potential w.r.t. the number of point charges is also thoroughly tested.

We have generated different types of embedded clusters. Some of them are shown below. The convergence of size of the QM region by varying the no. of atoms is tested as well.

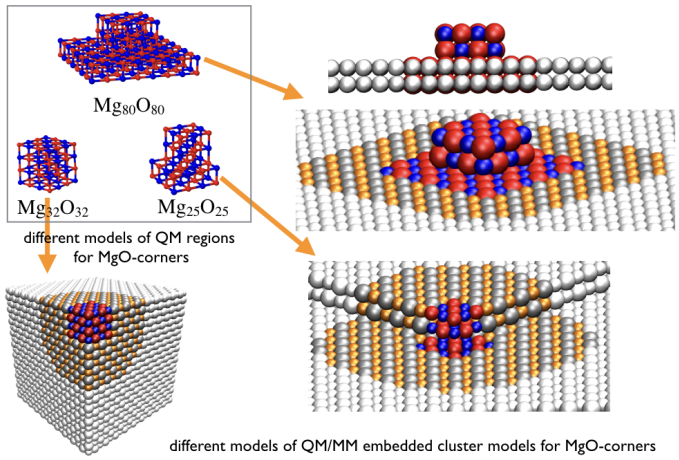

FIG. 1: Different types of embedded model clusters

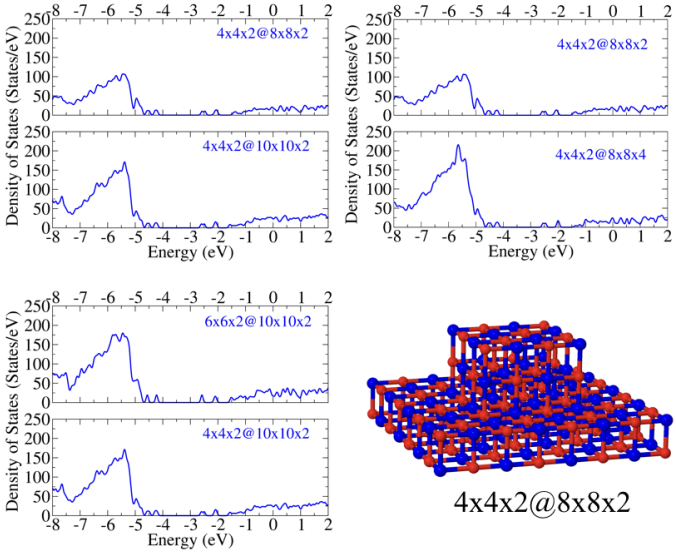

FIG. 2: Density of states of the respective periodic models at different sizes. The converged size of 4×4×2@8×8×2 slab is shown.

II. Convergence of 4×4×2@8×8×2 size for the periodic model

In order to validate our embedded model corner defect calculation w.r.t. periodic corner calculations, we have first created a periodic corner model. A 4×4×2 slab is placed on top of 8×8×2 slab. The size of the top slab (i.e. 4×4×2) as well as the bottom slab (i.e. 8×8×2) is converged by increasing the respective sizes. The resemblance in density of states confirms us the convergence of 4×4×2@8×8×2 size for the periodic model calculations.

III. The QM/MM model: MM parameter optimization and convergence w.r.t. to cluster size

The MM region is divided into an inner "active" (polarizable) part, where ions are allowed to relax their positions, and an outer part where ions are constrained to their lattice positions. Direct linkage of the field of MM point charges with the QM region generally results in a spurious over-polarization of the wavefunction (also described as charge leakage) towards the attractive cations of the immediately surrounding MM region. Therefore, cations (Mg sites) which are next neighbors to sites treated at the *ab initio* level are described by norm-conversing non-local pseudopotentials [3]. While maintaining the long-range potential of a point charge, the pseudopotential has no Coulomb singularity. Moreover, projector functions ensure orthogonalization to core states and thus provide appropriate scattering conditions across the QM region boundary.

The O sites in the active MM region are represented as a core (O_c) and shell (O_s) site, interacting via a harmonic potential. Mg sites in the active MM region interact via a Buckingham-type potential with O_c and O_s sites. We fit the interatomic-potential parameters for the MM region to match the lattice parameters and dielectric constant of the QM region (with the functional applied). The total energy of the system is defined as: $E^{\mathrm{tot}} = E^{\mathrm{QM}} + E^{\mathrm{MM}}$ and is minimized iteratively in the `ChemShell` environment [4, 5], connecting `FHI-aims` with the MM driver `GULP`[6]. In a given geometry `FHI-aims` evaluates E^{QM} and corresponding forces acting on all particles (QM atoms, embedding point charges, and pseudopotentials). The MM driver evaluates further forces on embedding point charges at the level of interatomic potentials, and together with the QM forces performs the geometry optimization. Full polarization response is calculated by relaxation of all QM atoms, pseudopotentials and MM particles within the active MM region. Long-range contributions beyond the active region are corrected for analytically.

Seamless embedding of the QM cluster within the surrounding MM regions relies on an accurate matching of the structural and electrostatic parameters in both regions. We use a polarizable force field for the description of the MM region, with a harmonic spring potential between oxygen core (c) and its shell (s) and a Buckingham short-range potential for the interaction between magnesium core and oxygen shells and among oxygen shells that augments Coulomb interaction between these particles. Together with the electric charge of the oxygen shell (q_s), the MM model has eight model parameters. (The charges of the oxygen core and shell add up to −2 to retain formal charge, respectively the charge of the magnesium core is fixed to +4.) Using a differential evolutionary algorithm [7] from the Python package `Inspyred 1.0`[8], we found a set of parameters (see Table I) which simultaneously reproduces the structural and static and high-frequency dielectric constants (see Table II) of the QM region. The correct description

of the dielectric properties allows to account for the full dielectric response within the active MM region by structural relaxation of all MM particles. In doing this, the precarious electric fields at the corner site as well as the polarization response to charged defects are captured efficiently in a large volume, generally not affordable on a hybrid functional level of theory.

k_{c-s} [in eV/Å^{-2}]	q_s [in e]
42.26	-2 .7089

	A [in eV]	ρ [in Å]	C [in eV Å^6]
O_s - O_s	21246.710	0.121	23.469
O_s - Mg	1262.651	0.309	18.560

TABLE I: Interatomic potential parameters, optimized to reproduce the bulk MgO DFT-HSE06 lattice parameter and static and high-frequency dielectric constants (see Table II).

The long range electrostatic background potential at the step and corner site was simulated by embedding the QM region in a large field of point charges, 7936 MM atoms for the corner and 12950 for the step site. In both cases this let to an electrostatic embedding potential converged to within 1 mV. The full electrostatic response is accounted for within a finite region (QM-region and active MM region). In the case of charged defects, the long-range polarization energy beyond the active MM region is significant and has to be added a posterori to the total energy of the system. The explicit formula depends on the geometry addressed. For the bulk and surface case analytic formulas are known [5], however not for the corner or step site. In general, the polarization energy has to be proportional to q^2, with q being the charge of the defect. Furthermore it decays with $1/R$, with R being the radius of the active region (QM-region and active MM region). Together with a factor which depends on the geometry and the dielectric constant the correction energy can be expressed as

$$\Delta E_{pol}[q] = -\frac{q^2}{R} f_{geo}(\epsilon) \quad . \tag{1}$$

For each geometry the factor $f_{geo}(\epsilon)$ has been determined through least square fitting to a series of QM/MM simulations with increasing R. All production runs were carried out with an active region of R=25 a_o, i.e. full relaxation of all QM-atoms and relaxation of all MM particles within a distance of 25 a_o from the defect. For this choice we obtain $\Delta E_{pol}[q] = -0.51 \cdot q^2 eV$ for the correction energies in the step case, and $\Delta E_{pol}[q] = -0.19 \cdot q^2 eV$ for the corner case, which is added to the calculated QM/MM total energy of the system.

For an accurate description of defect charging, the embedding scheme should closely reproduce the electronic structure of the corresponding extended system, in particular the position of the defect levels with respect to (w.r.t.) the bulk Fermi level. We check this by comparing the electronic structure of the embedded cluster model of an unmodified O-terminated corner with a periodic slab model. Since we focus on p-doped MgO, the Fermi level is set to the valence band maximum (VBM). The position of the highest occupied state (HOMO) for the corner defect w.r.t. the bulk Fermi level is determined as follows. First, the position of the Fermi level w.r.t. the vacuum level is calculated using the HSE06 functional. This is done by calculating the position of the Mg 1s core state in the third layer of a 5-layer MgO (100) slab w.r.t. vacuum. By aligning the positions of the Mg 1s core states in the slab and in the bulk, the position of the VBM w.r.t. vacuum is then calculated. The result is -7.5 eV. Next, the position of the HOMO w.r.t. vacuum is calculated from the embedded cluster model. To ensure that no artificial shift of the HOMO relative to the vacuum level is induced by the embedding, we compare the positions of the HOMO for both the embedded cluster and the periodic slab models of the pristine neutral corner, calculated with the PBE functional.

	a [in Å]	ϵ_o	ϵ_∞
Exp.	4.212 [9]	9.8 [10]	3.0 [11]
HSE06	4.219		2.8 [12]
MM (this work)	4.217	10.7	2.95

TABLE II: Lattice constant (a) as well as the static (ϵ_o) and high-frequency (ϵ_∞) dielectric constants of bulk MgO. Literature data from experiment and DFT-HSE06 calculations [12] are compared against our own calculations at the DFT-HSE06 level and with the parametrized force field for the MM region (see Table I).

The periodic model was converged in terms of the number of layers and lateral dimensions. The resulting difference is found to be about 0.2 eV. We conclude that we have an uncertainty of at most ±0.2 eV (depending on the type of corner) in the position of the defect levels w.r.t. the Fermi level due to embedding. This error has no qualitative effect on the calculated relative concentrations (see below).

with respect to the size of the QM/MM region has been demonstrated by calculating the formation energies of the 2+ oxygen vacancy at the step and corner site in larger QM clusters. For for the step site the formation energy calculated in a $Mg_{25}O_{24}^{2+}$ and in the $Mg_{42}O_{41}^{2+}$ cluster differed only by 0.06 eV at the level of HSE06. Also the corner site the formation energy calculated in a $Mg_{32}O_{31}^{2+}$ and in the $Mg_{50}O_{49}^{2+}$ cluster differed only by 0.08 eV.

IV. Validation of QM/MM model calculations w.r.t periodic boundary calculations

For an accurate description of defect charging, the embedding scheme should closely reproduce the electronic structure of the corresponding extended system, in particular the position of the defect levels w.r.t the bulk Fermi level. We check this by comparing the electronic structure of the embedded cluster model of an unmodified O-terminated corner with a periodic slab model (i.e. 4×4×2@8×8×2 slab as described above). Since we focus on p-doped MgO, the Fermi level is set to the valence band maximum (VBM). The position of the highest occupied state (HOMO) for the corner defect w.r.t the bulk Fermi level is determined as follows. First, the position of the Fermi level w.r.t the vacuum level is calculated using the HSE06 functional. This is done by calculating the position of the Mg 1s core state in the third layer of a 5-layer MgO (100) slab w.r.t vacuum. By aligning the positions of the Mg 1s core states in the slab and in the bulk, the position of the VBM w.r.t vacuum is then calculated. The result is -7.5 eV. Next, the position of the HOMO w.r.t vacuum is calculated from the embedded cluster model. To ensure that no artificial shift of the HOMO relative to the vacuum level is induced by the embedding, we compare the positions of the HOMO for both the embedded cluster and the periodic slab models of the pristine neutral corner, calculated with the PBE [13, 14] functional. The periodic model was converged in terms of the number of layers and lateral dimensions. The resulting difference is found to be about 0.2 eV. We conclude that we have an uncertainty of at most ±0.2 eV (depending on the type of corner) in the position of the defect levels w.r.t the Fermi level due to embedding.

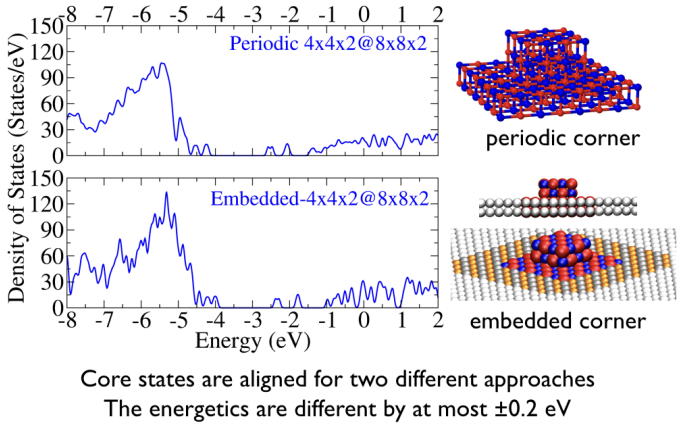

FIG. 3: Density of states for the defect level using two different approaches viz. periodic calculations (top) and embedded-cluster model (bottom).

V. Phase diagrams for unembedded clusters

We have tried to understand the relative stability of a set of medium-size parallelepipedal $[Mg_NO_{(x+N)})]^q$ clusters at various sizes [N = 18, 24, 32, 108] with a defect at one of the corners [x = -1(O-vacancy), 0(pristine), 1(O-ad-species), 2(O_2-ad-species)]. The charge states q is varied from -2 to +2 [q = -2, -1, 0, 1, 2]. Note that using our massively-parallel cascade genetic algorithm implementation [cGA], we have noticed that the corners of such parallelepipedal clusters, are the most active sites to create defects. Therefore, globally optimized structures of $[Mg_NO_{(x+N)})]^q$ clusters are generated by means of our our cGA implementation. We find that at a realistic temperatures and pressures (e.g., T = 300K, $p_{O_2} \sim 1$ atm) O or O_2-interstitial states at the oxygen corners of pristine $[(MgO)_N]^q$ clusters are favored at all studied charge states, over a wide range of electronic chemical potential μ_e. In fact, the interstitials are stable even at some values of μ_e, for which O-vacancies are preferred at flat (100) surfaces of doped MgO. Strikingly, this behaviour is also confirmed when some model clusters are embedded in a point-charge array, in order to mimic the realization of a corner defect (intersection of two step ridges) on an extended surface as shown in the main manuscript or the case embedded-$(MgO)_{25+x}^q$ below:

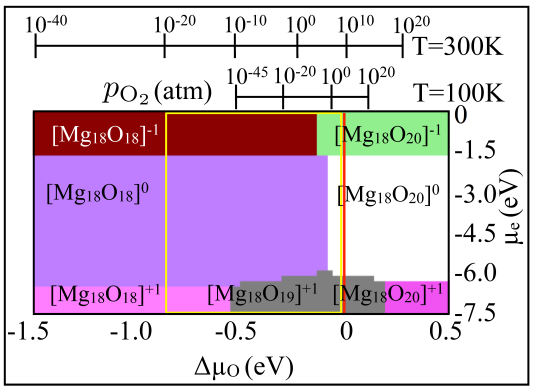

(a) $(MgO)^{q}_{18+x}$

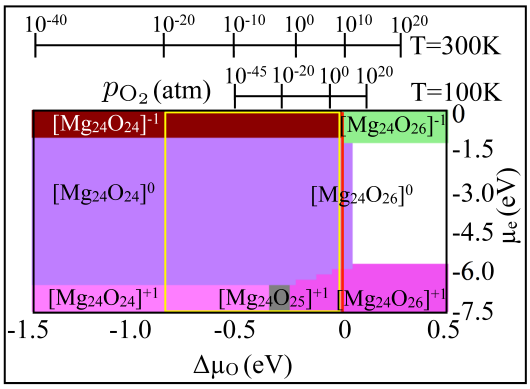

(b) $(MgO)^{q}_{24+x}$

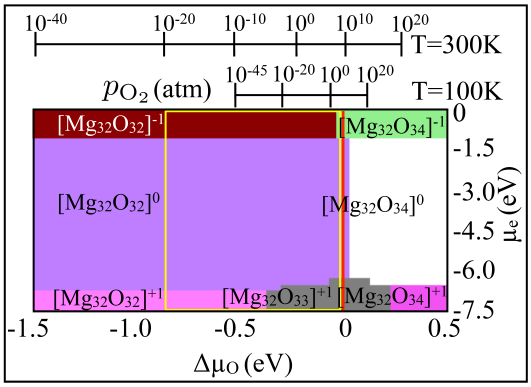

(c) $(MgO)^{q}_{32+x}$

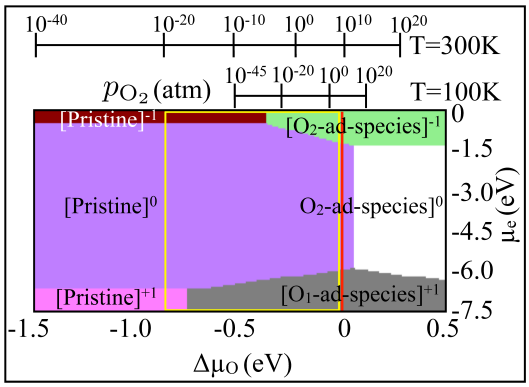

(d) embedded-$(MgO)^{q}_{25+x}$

VI. Concentration of defects and error estimation for μ_e=± 0.2 eV

Following figure shows the concentration of different kinds of defects at varying temperature and constant pressure. As it can be seen from comparing the concentrations of various kind of defects at different pressures, the estimated error of ±0.2 eV in the position of the defect levels w.r.t the electronic chemical potential has no qualitative effect on the calculated relative concentrations.

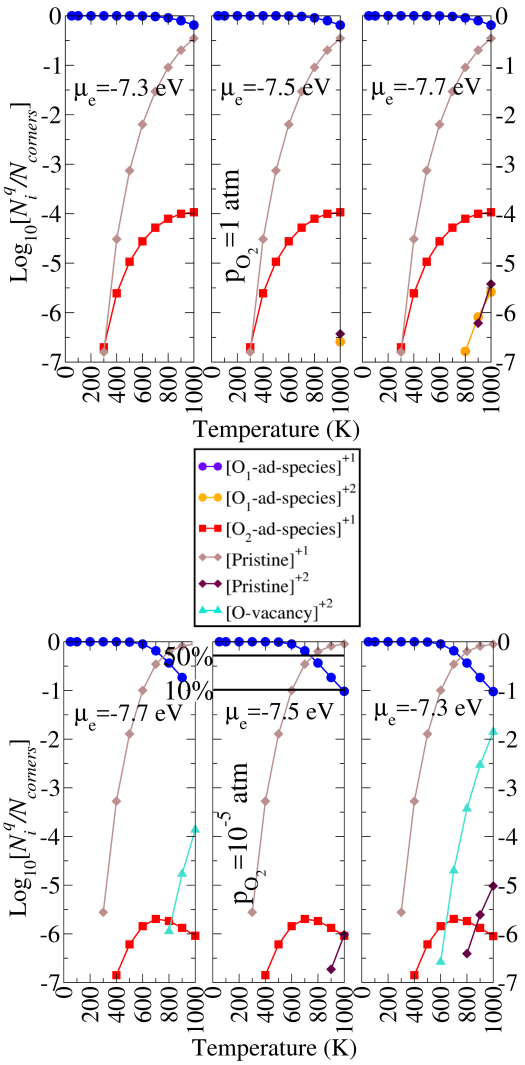

FIG. 4: Concentration of defect at $p_{O_2} = 1$ atm and $p_{O_2} = 10^{-5}$ atm.

[1] S. Bhattacharya, S. V. Levchenko, L. M. Ghiringhelli, and M. Scheffler, New Journal of Physics **16**, 123016 (2014), URL http://stacks.iop.org/1367-2630/16/i=12/a=123016.

[2] S. Bhattacharya, S. V. Levchenko, L. M. Ghiringhelli, and M. Scheffler, Phys. Rev. Lett. **111**, 135501 (2013).

[3] L. Kleinman and D. M. Bylander, Phys. Rev. Lett. **48**, 1425 (1982).

[4] P. Sherwood, A. H. de Vries, M. F. Guest, G. Schreckenbach, C. R. A. Catlow, S. A. French, A. A. Sokol, S. T. Bromley, W. Thiel, A. J. Turner, et al., J. Mol. Struct. (Theochem.) **632**, 1 (2003).

[5] A. A. Sokol, S. T. Bromley, S. A. French, C. R. A. Catlow, and P. Sherwood, Int. J. Quantum Chem **99**, 695 (2004).

[6] J. D. Gale, J. Chem. Soc., Faraday Trans. **93**, 629 (1997).

[7] R. Storn and K. Price, J. Global Optim. **11**, 341 (1997), ISSN 0925-5001, URL http://dx.doi.org/10.1023/A%3A1008202821328.

[8] *inspyred 1.0 documentation*, accessed: 2014-05-06.

[9] D. R. Lide, *CRC Handbook of Chemistry and Physics, 79th ed.* (CRC Press, Boca Raton, FL, 1998/1999).

[10] R. A. Bartels and P. A. Smith, Phys. Rev. B **7**, 3885 (1973), URL http://link.aps.org/doi/10.1103/PhysRevB.7.3885.

[11] H. Grünewald, Angew. Chem. **78**, 912 (1966), ISSN 1521-3757, URL http://dx.doi.org/10.1002/ange.19660781827.

[12] G.-X. Zhang, A. Tkatchenko, J. Paier, H. Appel, and M. Scheffler, Phys. Rev. Lett. **107**, 245501 (2011), URL http://link.aps.org/doi/10.1103/PhysRevLett.107.245501.

[13] J. Perdew, K. Burke, and M. Ernzerhof, Phys. Rev. Lett. **77**, 3865 (1996).

[14] J. Perdew, K. Burke, and M. Ernzerhof, Phys. Rev. Lett. **78**, 1396 (1997).